Photoacoustic Nanodroplets for Oxygen Enhanced Photodynamic Therapy of Cancer

Marvin Xavierselvan, Jason Cook, Jeanne Duong, Nashielli Diaz, Kimberly Homan, Srivalleesha Mallidi

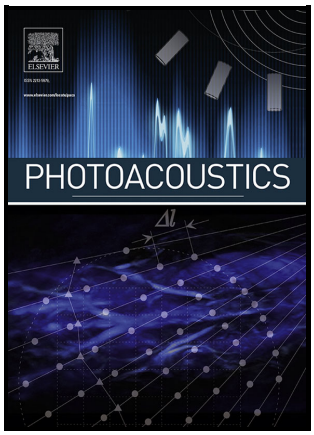

PII: S2213-5979(21)00066-5

DOI: https://doi.org/10.1016/j.pacs.2021.100306

Reference: PACS100306

To appear in: *Photoacoustics*

Received date: 31 March 2021
Revised date: 7 September 2021
Accepted date: 21 September 2021

Please cite this article as: Marvin Xavierselvan, Jason Cook, Jeanne Duong, Nashielli Diaz, Kimberly Homan and Srivalleesha Mallidi, Photoacoustic Nanodroplets for Oxygen Enhanced Photodynamic Therapy of Cancer, *Photoacoustics,* (2021) doi:https://doi.org/10.1016/j.pacs.2021.100306

Photoacoustic nanodroplets for oxygen enhanced photodynamic therapy of cancer

Marvin Xavierselvan[1], Jason Cook[2], Jeanne Duong[1], Nashielli Diaz[1], Kimberly Homan[2] and Srivalleesha Mallidi[1,3]

[1]*Department of Biomedical Engineering, Tufts University, Medford, Massachusetts 02155*

[2]*NanoHybrids Inc., Austin, TX 78744*

[3]*Wellman Center for Photomedicine, Massachusetts General Hospital, Boston, MA 02114*

Corresponding Author:
Srivalleesha Mallidi, PhD
Assistant Professor, Department of Biomedical Engineering,
Tufts University, Medford MA 02155
srivalleesha.mallidi@tufts.edu

Keywords

Photoacoustic imaging, photodynamic therapy, perfluorocarbon nanodroplets, hypoxia, image guided PDT

Abbreviations

BPD, benzoporphyrin derivative; DLS, dynamic light scattering; DPPC, 1,2-dipalmitoyl-sn-glycero-3-phosphocholine; DSPE-mPEG, 1,2-distearoyl-sn-glycero-3-phosphoethanolamine-N-[methoxy(polyethylene glycol)-2000]; H&E, hematoxylin and eosin; HbT, total hemoglobin; ICG, indocyanine green; IF, immunofluorescence; MTT, 3-(4,5-dimethylthiazol-2-yl)-2,5-diphenyltetrazolium bromide; NIR, near infrared radiation; $^1O_2$, singlet oxygen; PA, photoacoustic; PBS, phosphate buffered saline; PDT, photodynamic therapy; PFC, perfluorocarbon; PFP, perfluoropentane; pO_2, partial pressure of oxygen; PS, photosensitizer; ROS, reactive oxygen species; SOSG, singlet oxygen sensor green; StO_2, oxygen saturation; TBAI, tertbutylammonium iodide;

Abstract

Photodynamic therapy (PDT) is a well-known cancer therapy that utilizes light to excite a photosensitizer and generate cytotoxic reactive oxygen species (ROS). The efficacy of PDT primarily depends on the photosensitizer and oxygen concentration in the tumor. Hypoxia in solid tumors promotes treatment resistance, resulting in poor PDT outcomes. Hence, there is a need to combat hypoxia while delivering sufficient photosensitizer to the tumor

for ROS generation. Here we showcase our unique theranostic perfluorocarbon nanodroplets as a triple agent carrier for oxygen, photosensitizer, and indocyanine green that enables light triggered spatiotemporal delivery of oxygen to the tumors. We evaluated the characteristics of the nanodroplets and validated their ability to deliver oxygen via photoacoustic monitoring of blood oxygen saturation and subsequent PDT efficacy in a murine subcutaneous tumor model. The imaging results were validated with an oxygen sensing probe, which showed a 9.1 fold increase in oxygen content inside the tumor, following systemic injection of the nanodroplets. These results were also confirmed with immunofluorescence. *In vivo* studies showed that nanodroplets held higher rates of treatment efficacy than a clinically available benzoporphyrin derivative formulation. Histological analysis showed higher necrotic area within the tumor with perfluoropentane nanodroplets. Overall, the photoacoustic nanodroplets can significantly enhance image-guided PDT and has demonstrated substantial potential as a valid theranostic option for patient-specific photodynamic therapy-based treatments.

1. Introduction

Photodynamic therapy (PDT), a treatment modality that utilizes light energy and photosensitizer (PS) molecules, has been employed successfully to treat several malignant tumors such as brain tumors, oral cavity tumors and esophageal malignancies [1, 2]. Particularly PDT is sought out for its highly localized effect and excellent post-therapy mucosal healing and recently PDT efficacy in treating T1-T2 early-stage oral cancer lesions has been demonstrated by us and several other groups [3-6]. It is common for large or late-stage tumors to encompass hypoxic regions, where typically the PDT process is ineffective as the generation of cytotoxic reactive oxygen species (ROS) requires oxygen to react with the PS molecule. Such a mechanism, referred to as Type-II PDT, is a common mode of action for many PS molecules used in the clinic currently; therefore, their efficacy is predominantly determined by the oxygen content in the photodynamic action vicinity [2, 7].

Several studies have demonstrated poor outcomes using PDT with the Type-II PS molecules in hypoxic tumors [8, 9], as with radiation and chemotherapy [9-12]. Increasing tumor oxygenation will improve the therapeutic efficacy of PDT while increasing tumor sensitivity for subsequent therapies. Previously, this shift on tumor oxygen content was achieved through hyperbaric oxygenation methods in which the inhalation of pure oxygen leads to a decrease of hypoxic content within the tumor [13-15]. Unfortunately, inhaling excessive oxygen, i.e., overall systemic delivery, can have harmful side effects such as: seizures, progressive myopia, nuclear cataract,

pulmonary edema, alveolar hemorrhage [16], interstitial fibrosis, retrolental fibroplasia and hypoglycemia [17, 18]. Other methods such as oxygen-carrying nanoparticles or MnO_2 nanoparticles have been developed to release oxygen inside the tumor, following either a change in pH [19] or reaction with H_2O_2 [20]. However, shortcomings of these nanoparticles include the absence of spatiotemporal triggering during oxygen delivery, lack of imaging contrast for real time monitoring, and inclusion of non-clinically approved optical contrast agents during fabrication. Few studies have utilized clinically approved ultrasound contrast agents (microbubbles) to deliver oxygen and drugs [21-25]. Nonetheless, microbubbles owing to their large size (1-10 μm) do not efficiently extravasate through leaky blood vessels to localize in the tumor region resulting in lower efficacy of delivering oxygen to the hypoxic regions [26, 27]. The limitation of microbubbles led to the development of nanobubbles and nanodroplets as reviewed elsewhere [28]. Both have a size range of 40-200 nm and similar preparation methods. The distinction is that nanobubbles have gas cores (gas-liquid colloid) while nanodroplets have liquid cores (liquid-liquid colloid) [24, 26, 27]. In our study, we used nanodroplets fabricated with perfluorocarbons (PFCs) to deliver oxygen, PS and a photoacoustic (PA) contrast agent to the tumors. PFCs are particularly apt for carrying oxygen [29-31] as they have high oxygen solubility and carrying capacity [32, 33], are biocompatible organic compounds [34] which are metabolically inert, and can be triggered remotely to deliver their contents [35-37]. Additionally, reports have shown that the lifetime of singlet oxygen ($^1O_2$) in perfluorocarbon is longer than in the cellular environment or in water [30]. Therefore, the advantage of using PFC nanodroplets for oxygen and PS delivery is that they both will be in the same vicinity for photodynamic action to occur, resulting in improved treatment outcomes [38, 39].

In addition to co-delivery of oxygen and PS, another advantage offered by nanodroplets is the ability to spatiotemporally trigger the oxygen release while monitoring nanoparticle uptake and oxygenation changes in the tumor in real time. To facilitate these properties, we synthesized nanodroplets containing PFC and indocyanine green (ICG), an optical diagnostic agent that has peak light absorption in the near infrared (NIR) range. ICG is a clinically approved dye in medical diagnostics for measuring cardiac output, hepatic function and ophthalmic angiography [40]. Given its high absorption compared to endogenous chromophores such as blood and melanin, and its ability to generate heat when excited, ICG has been extensively used as a PA contrast agent for molecular imaging [41, 42]. In addition to providing imaging contrast, ICG can also initiate PFC vaporization via laser irradiation at 800 nm, a wavelength at which ICG has high optical absorption compared to endogenous chromophores. The spatially localized laser irradiation in a particular region of interest initiates PFC vaporization

leading to localized drug delivery [43] . Furthermore, the temporal control of drug release can be achieved by irradiating the PFC droplets at a time when the uptake of the PFC particles is maximum in the tumor region. Previous investigations observed that PFC loaded with ICG can act as a dual contrast agent for both ultrasound [34, 44] and PA imaging [34]. Specifically, PA imaging is a hybrid imaging modality wherein the tissue is irradiated with nanosecond pulsed laser light [45]. Any absorbers in the light path transiently undergo thermoelastic expansion and contraction, generating an acoustic wave. The acoustic wave can be detected by an ultrasound transducer which, in turn, displays images of optical absorption within the tissue. PA imaging can provide information about the oxygen saturation (StO_2) and total hemoglobin content (HbT) without the use of external contrast agents [46] since oxygenated and deoxygenated hemoglobin have optical absorption at different wavelengths [47]. As a result, PA imaging has been used along with PDT for monitoring the tumor and predicting the treatment outcomes [46].

In this study, we constructed nanodroplets specifically to enhance PDT in hypoxic tumors. The nanodroplets contain perfluoropentane (PFP) saturated with oxygen, ICG, and benzoporphyrin derivative (BPD) for PA-guided PDT (Fig. 1A). The presence of ICG in our nanodroplets enables the laser-triggered spatiotemporal delivery of oxygen for PDT while simultaneously providing contrast for PA imaging. The therapeutic aspect of our nanodroplets is attributed to BPD, an FDA approved drug for the treatment of subfoveal choroidal neovascularization. BPD and ICG do not impact each other's performance when employed in optimal concentrations as we recently demonstrated [48]. Our *in vitro* and *in vivo* murine tumor model studies prove that PDT efficacy can be significantly improved with specific light-based triggering of ICG at its peak absorbance to deliver oxygen and the photosensitizer at the right place and at the right time. The novel formulation of PFP nanodroplets described here encapsulates FDA approved PDT and imaging components and therefore, has tremendous clinical translation potential for oxygenating hypoxic tumors, not only for PDT, but also for other therapies such as radiation and chemotherapy whose efficacy can be enhanced in a hypoxic environment.

2. Material and Methods

2. 1 Synthesis of PFP nanodroplets

The PFP nanodroplets (shown in Fig. 1a) were formed using PFP in water emulsion. United States Pharmacopeia (USP) Reference Standard grade ICG (MilliporeSigma, Burlington, MA) was solubilized into chloroform using

tertbutylammonium iodide (TBAI) (MilliporeSigma, Burlington, MA). A 1 mg/mL aqueous solution of ICG was mixed with a solution of 3 mg/mL TBAI in chloroform at a 1:3 volume ratio. After shaking at 100 rpm overnight, the chloroform phase containing ICG was extracted. A combination of 1,2-dipalmitoyl-sn-glycero-3-phosphocholine (DPPC), 1,2-distearoyl-sn-glycero-3-phosphoethanolamine-N-[methoxy(polyethylene glycol)-2000] (DSPE-mPEG), cholesterol (Avanti Polar Lipids, Alabaster, AL), ICG in chloroform, and benzoporphyrin derivative (MilliporeSigma, Burlington, MA) were added to a 100mL round-bottom flask at a molar ratio of 88:2:3:2:5, respectively. After rotovaping for 2 hours, the lipid cake was hydrated using water to yield a final lipid concentration of 10 mg/mL. To this solution, 0.25 ml of n-perfluoropentane (Exfluor, Round Rock, TX) for every 1 ml of hydrated lipid solution was added. The solution was sonicated in a bath sonicator for 10 seconds, followed by 1 minute in an ice bath to minimize heating effects. This sonication procedure was repeated until the desired size distribution was achieved. Once synthesized, the particles were stored at 4°C for up to 12 weeks before use. Oxygen was encapsulated into the PFP nandroplets immediately prior to use. To accomplish this, the PFP nanodroplets were warmed to room temperature and oxygenated by gently bubbling the solution with 100% oxygen gas (1 liters/minute for 5 minutes). During this process some of the gas is dissolved into the liquid solution and is then captured by the liquid PFP in the nanodroplets. Because of liquid PFP's high solubility of oxygen [33], the PFP nanodroplets retain the oxygen and do not release until the PFP is vaporized with laser irradiation.

2. 2 Characterization of PFP nanodroplets

The size, size distribution, and zeta potential of PFP nanodroplets were characterized using the Dynamic Light Scattering (DLS) System (Zetasizer Nano ZS, Malvern Panalytical). UV Visible spectrophotometer (Evolution 300, Thermo Fischer Scientific) was used to measure the absorbance spectra of various PFP nanodroplets and quantify the concentration of BPD and ICG.

2. 3 Photoacoustic imaging of PFP nanodroplets

PA imaging was performed using a Vevo 2100 LAZR Imaging System (VisualSonics, FUJIFILM) equipped with a 21 MHz LZ-250 ultrasound transducer. PA spectra and stability tests were conducted in a water tank containing polypropylene tubes filled with samples. PA spectral imaging was performed from 680 nm to 950 nm. The laser was calibrated prior to every experiment. The PFP particles were also imaged using the single wavelength pulsed irradiation at 800 nm (fluence of ~30 mJ) and 690 nm (fluence of ~25 mJ). The PA signals from the particles were

quantified using Vevo Lab software (FUJIFILM VisualSonics). A region of interest (ROI) (1.45 mm^2 area) was drawn around the top half of the tube, maintaining the same parameters throughout the entirety of the analysis, across various solutions.

2. 4 Singlet oxygen measurements

Singlet oxygen production was calculated using the commercially available Singlet Oxygen Sensor Green (SOSG) kit (Invitrogen). The SOSG was dissolved in methanol and the working solution was prepared in ultrapure water. Free BPD, BPD-PFP, ICG-PFP and BPD+ICG-PFP (with different loading ratios of BPD and ICG) nanodroplet solutions were diluted to a concentration of 5 µM in phosphate-buffered saline (PBS) supplemented with 10% FBS. The SOSG was added to the solutions at a concentration of 5 µM and the solutions were irradiated with a 690 nm laser at an irradiance of 150 mW/cm^2 and a total light dose of 20 J/cm^2. After irradiation, the SOSG fluorescence intensity was recorded using the Spectramax M5 plate reader using 460 nm excitation with a 515 nm cut-off filter and emission at 525 nm. For testing the efficiency of oxygen in carrying BPD-PFP nanodroplets to produce singlet oxygen in hypoxic conditions, nitrogen gas was flushed through the environment for 5 minutes to reduce the oxygen concentration. Following this, the solution was irradiated and SOSG fluorescence was measured.

2. 5 Cell culture

Human Squamous Cell Carcinoma (FaDu Cells) were cultured in Eagle's Minimum Essential Medium supplemented with 10% fetal bovine serum (FBS, Gibco) and 1% antibiotics (Penicillin and Streptomycin 1:1 v/v, Corning), and maintained at 37 $^{\circ}$C and 5% CO_2. The cells were sub-cultured and used for experiments while they were in the exponential growth phase.

2. 6 Cellular uptake and localization studies

For cellular uptake, FaDu cells were seeded in a 6 well plate at a density of 1.5 x 10^5 per well. The following day, the cells were incubated with fresh cell culture media containing BPD-PFP and ICG-PFP at concentrations of 250 nM and 1000 nM, respectively. After 90 minutes of incubation, the media was removed, and cells were washed with ice cold PBS twice and lysed using 1% Triton X-100. The cell lysate was centrifuged to remove the precipitate and the lysate was used to measure the BPD and ICG fluorescence using the Fluoromax 3 (Horiba) and converted to moles of PS based on appropriate standards. Bicinchoninic acid assay was performed to calculate the cellular

protein and used to normalize the BPD and ICG concentrations. For subcellular localization studies, FaDu cells were cultured overnight on 35 mm glass bottom dishes at a density of 75,000 cells per dish and incubated with free PS and nanodroplet formulations for 24 hrs. The cells were either stained with MitoTracker Green (M7514, Invitrogen) for 30 mins or LysoTracker Green (DND-26, Invitrogen) for 60 minutes at 37 $^{\circ}$C. The cells were later washed with PBS and stained with Hoechst prior to imaging with EVOS M7000 fluorescence imaging system using a 40x objective. Appropriate LED light cubes (Hoechst – DAPI light cube, MitoTracker and LysoTracker – GFP light cube, BPD – Qdot 705 light cube, ICG – Invitrogen Cy7 light cube) were used according to the fluorophore properties. Colocalization analysis of fluorescence images was performed in MATLAB [49]. The fluorescence images were binarized using Otsu threshold method. Within an image, pixels exhibiting both PS and the organelle tracker were assigned a value of 1 and summed to obtain the total number of colocalization pixels. The percent colocalization was calculated by dividing the total number of colocalization pixels to the total number of pixels that had PS fluorescence.

2. 7 Phototoxicity of the nanodroplets

To test the toxicity of the nanodroplets, FaDu cells were seeded in 35 mm dish at a density of 1.5 x 10^5 cells per dish. The following day, the cells were washed with PBS and fresh cell culture media containing free BPD and BPD-PFP at the concentration of 250 nM, 500nM, 1 µM, 2 µM, 5 µM, 10 µM. After 90 mins of incubation, the media was replaced with fresh cell culture media and the cells were incubated for 24 hours. The percentage of viable cells was calculated using 3-(4,5-dimethylthiazol-2-yl)-2,5-diphenyltetrazolium bromide (MTT, Thermofisher). The media was replaced with fresh cell culture media containing MTT (0.25 mg/mL) and incubated for 60 minutes. After the media was removed, formazan crystals formed in the cells were dissolved with DMSO, and absorbance was measured at 570 nm. The absorbance was normalized with untreated controls to obtain percent viability.

For evaluating phototoxicity, FaDu cells were seeded in 35 mm dish at a density of 1.5 x 10^5 cells per well. The following day, the cells were incubated with media containing BPD-PFP, ICG-PFP, BPD+ICG-PFP (with different loading ratios of BPD and ICG) and a liposomal formulation of BPD. The BPD concentration was maintained at 250 nM and ICG concentration was maintained at 1000 nM. After 90 mins of incubation, the media was replaced with fresh cell culture media and PDT was performed with a 690 nm laser at an irradiance of 150 mW/cm^2 and a total light dose of 1 and 2.5 J/cm^2. After PDT, the cells were incubated for 24 hours, prior to

assessing cell viability using the MTT assay.

2. 8 Murine tumor models and *in vivo* therapy efficacy

All animal experiments were performed in compliance with the Institutional Animal Care and Use Committee (IACUC) of Massachusetts General Hospital (MGH) and Tufts University. Swiss nu/nu mice were raised in aseptic conditions in the institution's animal facility with 12h light and dark cycles, respectively. During the experiment, the animals were observed closely. Animals were humanely euthanized if they showed signs of pain/discomfort, their tumor reached 20 mm in any one dimension, they experienced loss of 20% body weight from the start of the experiment, or if their tumor became ulcerated.

The FaDu cells were collected by trypsinization, and the cells were suspended in a mixture of Matrigel and PBS in 1:1 v/v at a density of 1 million cells per 100 µL and injected subcutaneously into the mice. For determining the *in vivo* efficacy of the PFP, ICG-PFP, Visudyne (liposomal formulation of BPD used in clinics), BPD-PFP, BPD+ICG-PFP 1:1 and BPD+ICG-PFP 1:2 (0.5 mg/kg of BPD equivalent) were injected into mice via tail vein. The tumor was irradiated with a 690 nm laser at an irradiance of 40 mW/cm^2 and a total light dose of 100 J/cm^2 90 minutes after systemic administration of the nanodroplets. The animals were monitored biweekly for up to 15 days, throughout which tumor volume was measured with 3D ultrasound imaging. For investigating the PDT response, tumors were treated with BPD+ICG-PFP 1:1 (0.5 mg/kg of BPD equivalent) and 690 nm laser with same irradiance and fluence as the previous experiment. Tumors were harvested 24 hours later and embedded in optimal cutting temperature (OCT) compound for histological examination.

2. 9 *In vivo* tumor oxygenation measurements

The oxygen sensor of the oxygen monitor system (Oxylite, Oxford Optronix Inc.) was inserted into the tumors using a 23-gauge sterile needle. Once the electrode was inserted into the tumor, it was left undisturbed until the pO_2 stabilized. The transducer was positioned to image a plane adjacent to the electrode to avoid any image artifacts. After 5 minutes, StO_2 PA imaging (750/850 nm; fluence of ~35 mJ) and PA imaging at 800 nm was performed. Then BPD+ICG-PFP 1:1 nanodroplets in PBS (1 mg/kg of BPD equivalent) was administered via tail vein injection without moving the mice or the transducer. The tumor oxygenation was monitored continuously throughout this procedure with both Oxylite and StO_2 PA imaging along with PA imaging at 800 nm for ICG contrast in the tumor. In a separate experiment, mice bearing FaDu xenografts were administered with PBS or BPD+ICG-PFP 1:1 via tail

vein injection. After an interval of 30 minutes, pimonidazole (Hypoxyprobe Inc.) was administered at a dose of 60 mg/kg and 60 minutes later the mice were euthanized. The tumors were then collected and embedded in OCT for histological examination of hypoxic regions.

2. 10 *In vivo* fluorescence imaging of nanodroplet biodistribution

After the tumor oxygenation measurements, mice (under anesthesia) were scanned for ICG's fluorescence using IVIS® Lumina Series III *In Vivo* imaging system (Perkin Elmer Inc) at different time intervals using 780 nm excitation filter and 840 nm emission filter. After the whole-body imaging, at 24 hours post tail vein injection of nanodroplets, mice were euthanized, the tumor and other major organs (kidneys, liver, spleen, lungs, and heart) were harvested and imaged with the IVIS fluorescence imaging system to quantify ICG fluorescence. Autofluorescence and background were subtracted from each organ with data from an untreated mouse. Quantification of the fluorescence signal from the region of interest was performed using Living Image software (PerkinElmer).

2. 11 Histology

The OCT embedded tumors were cryosectioned to obtain 10 µm thick sections that were stained with hematoxylin and eosin (H&E). For immunofluorescence (IF) staining, the cross sections were fixed in 1:1 acetone and methanol solution, air dried for 30 minutes, washed with PBS and blocked with SuperBlock blocking buffer (Thermo Scientific) for 30 minutes. Primary antibody (R&D Mouse/Rat CD31/PECAM-1 Polyclonal Goat IgG Cat: AF3628; 1:4 dilution) for targeting vasculature and antibody (Hypoxyprobe Red549 Kit HPI Cat: HP7-100; 1:50 dilution) against pimonidazole adducts was added to the sections and incubated overnight at 4 °C. Later, primary antibody is washed off with PBS and secondary antibody (NorthernLights™ Anti-goat IgG-NL637 Cat: NL002; 1:50 dilution) was added to tissue sections and incubated for 2 hours at room temperature. The sections were then washed in PBS and the nuclei were counterstained and mounted with DAPI SlowFade Gold Antifade Mountant (Thermo Scientific Cat: S36939). The slides were imaged with 20x objective using EVOS M7000 fluorescence imaging system. Throughout the acquisition and processing of all H&E and IF images, brightness and contrast levels were kept at the same level.

2. 12 Statistical analysis

Data analysis was performed using GraphPad Prism 8. The results are reported as mean ± standard error of the

mean (S.E.M). The specific statistical tests used on data are mentioned in the figure captions. *P* value less than 0.05 is considered statistically significant.

3. Results and discussion

3. 1 Synthesis and characterization of PFP nanodroplets

PFP nanodroplets, regardless of ICG or BPD content, have hydrodynamic diameters of 204.5 nm ± 17.3 nm and a polydispersity index of 0.140 ± 0.022 (Data was obtained from 10 independent batches). The representative size distribution of the nanodroplets of all variations is shown in Fig. 1b. Although PFP have low boiling point (29 °C), the Laplace pressure imposed at the particle boundary makes PFP a superheated liquid at 37 °C. Because of the Laplace pressure, PFP remains stable even at physiological temperature [34, 50-52]. Furthermore, the nanodroplets (fabricated with either single dye or both ICG and BPD) were stable in PBS for six weeks when stored at 4 °C and showed no significant change in their diameter (Fig. 1c). Figures 1d-f display the absorption spectra of BPD-PFP (red solid line), ICG-PFP (green solid line) and BPD+ICG-PFP (blue solid line) particles along with the absorption spectra of unbound free BPD and ICG (gray solid line) as a control reference. The characteristic peaks of BPD and ICG at 690 nm and 800 nm wavelengths were observed in BPD-PFP and ICG-PFP graphs, respectively. ICG in PFP shows a bathochromic shift due to the refractive index of the phospholipid coating and the close interaction between ICG molecules with PFP. The distinct peaks of BPD and ICG were observed in the spectra of BPD+ICG-PFP particles confirming the successful loading of the two dyes within our nanodroplets. The red shift of ICG remains which helps to spectrally differentiate BPD from ICG. PA signal generation is dependent on optical absorption properties of the tissue. As expected, the PA spectra of the nanodroplets are represented by black dots (Fig. 1d-f) that overlap with the absorption spectra. The characteristic peaks of BPD and ICG can also be distinguished through PA spectra in BPD +ICG-PFP solution.

3. 2 Photoacoustic imaging of PFP nanodroplets

PA images (800 nm wavelength irradiation) of the nanodroplet solution placed in a tube are shown in Fig. 2a. We chose 800 nm wavelength irradiation as the nanodroplets have an absorption peak at this wavelength due to the presence of ICG. PFP and BPD-PFP (Fig. S1) showed very low PA signal, similar to the PBS control due to lack of ICG in the particles. On the other hand, ICG-PFP and BPD+ICG-PFP showed a large PA signal upon laser

irradiation. Given that the top of the tube received the laser irradiation (due to reflection mode PA setup of Vevo LAZR system), high PA signal can only be observed in the specified top location. Furthermore, upon continuous imaging at 800 nm, we observed a gradual exponential decrease in the PA signal intensity. Fig. 2b shows the normalized PA signal for ICG-PFP and BPD+ICG-PFP (normalized to time t=0 seconds). This exponential decrease in signal is due to the vaporization of PFP droplets achieved by exciting ICG. Previous study by Hannah et. al., showed that the liquid to gas phase transition of ICG-PFP when excited with a laser pulse demonstrates with an initial increase in PA signal followed by decrease and stabilization of the PA signal [34]. A high frame rate (20 frames/second) imaging system was utilized to capture the transient increase in PA signal. We were only able to capture the exponential decrease of PA signal post laser irradiation due to low frame rate (5 frames/second) of the system used in the study. Our results were in agreement with data shown by Hannah et. al. [34].

Furthermore, ICG in free form (i.e., not encapsulated within PFP nanodroplets), PFP nanodroplets alone, or PFP nanodroplets in presence of BPD without ICG do not show this exponential decrease in PA signal at either 690 nm or 800 nm (Figs. S1 and S2b). This suggests ICG is crucial to burst open the nanodroplets to trigger the release of oxygen. To demonstrate that ICG in the PFP particles is not excited by the 690 nm laser (excitation peak for BPD), we repeated the experiment with 690 nm pulsed laser irradiation (Fig. 2c). The photoacoustic images obtained at 690 nm irradiation are shown in Fig. S2a. The PA signal for the control group, PFP alone, was very low and not statistically different from the baseline of PBS. The change in the PA signal at 690 nm wavelength irradiation for BPD-PFP, ICG-PFP and BPD+ICG-PFP were very minimal (Fig. S2b). Compared to the ~50% decrease of PA signal within 100 seconds of 800 nm pulsed irradiation, ICG-PFP and BPD+ICG-PFP showed less than 15% and 25% decrease in PA signal respectively, at 690 nm irradiation for the same amount of time. This decrease in PA signal is negligible and could be due to some minimal nanodroplet popping events as ICG has low absorption at this wavelength.

3. 3 Generation of singlet oxygen by photoacoustic nanodroplets

SOSG is a commercially available probe known for its high sensitivity in detecting singlet oxygen species. SOSG fluoresces in the presence of singlet oxygen in an aqueous environment. BPD in free form as well as when encapsulated in the PFP nanodroplets had similar SOSG fluorescence with no irradiation and in the absence of SOSG. Upon irradiation, no significant differences in SOSG fluorescence increase were observed for free BPD and

BPD-PFP in normal conditions, due to the abundant availability of oxygen in the environment. In contrast, BPD-PFP produced a significantly higher singlet oxygen as opposed to free BPD (Fig. 3a) in hypoxic environment (nitrogen bubbled PBS solution). ICG-PFP did not produce any singlet oxygen upon irradiation (Fig. S3).

Following the successful testing of BPD-PFP nanodroplets, the other nanodroplet variants with different ratio of ICG and BPD were tested for singlet oxygen production. The concentration ratio of the two different dyes, especially when being integrated in one nanoplatform is very important, as BPD and ICG have an overlapping absorption spectra around 690 nm-720 nm wavelength range. In our previous work [48], we showed that BPD's phototoxicity is not impacted by the presence of ICG when the dyes are in their free form (i.e., not encapsulated in nanoparticles). Here in Fig. 3b we show that the singlet oxygen production varies based on the BPD:ICG ratio. BPD and ICG were loaded into BPD+ICG-PFP nanodroplets with different starting concentrations ranging from 1:1 molar ratio of BPD:ICG to 1:4. We observed a significant decrease in the production of singlet oxygen when the nanodroplets were loaded with four times as much ICG as BPD. No significant differences were observed between BPD:ICG ratio of 1:1 or 1:2. This data highlights the importance of optimizing the ratio of dyes when encapsulating within a nanoentity, especially those with overlapping absorption spectra meant for PA guided PDT applications.

3. 4 Cellular uptake of nanodroplets

We compared the uptake of free PS and nanodroplet formulations in FaDu cells. The nanodroplet incubation time was 90 minutes, similar to previous studies with Liposomal BPD formulations [53, 54]. Quantitatively, we observed that BPD-PFP and BPD+ICG-PFP showed significantly higher uptake than free BPD (Fig. 4a) while free ICG and nanodroplet formulations of ICG had similar cellular uptake (Fig. 4b). BPD (free form) enters the cell via diffusion through the cell membrane [55, 56]. In contrast, nanodroplets enter the cells via clathrin- mediated endocytosis, a common route for nanoparticles of size greater than 100 nm [57-60]. Given the differences in cellular uptake of BPD, we observe an increase in BPD uptake with nanodroplets formulation. On the other hand, ICG in free form also localizes in cells through clathrin-mediated endocytic pathway [61, 62]. Hence, we do not observe any difference in the cellular uptake of ICG in free or nanodroplets formulations.

BPD (free form) localizes in mitochondria [63, 64]. To evaluate cellular localization of BPD in nanodroplet formulations, we incubated cells with BPD-PFP, stained with MitoTracker, and performed fluorescence imaging (Fig. 5a). Free BPD and BPD-PFP showed strong fluorescence signal throughout the cell. The pseudo-colored

yellow fluorescence signal on the merged image (Fig. 5a, column four) represents the colocalization of the MitoTracker green signal with the red BPD fluorescence signal, qualitatively indicating the uptake of BPD in the mitochondria. To determine the cellular localization of free ICG or its nanodroplets formulation, we stained cells incubated with free ICG or ICG-PFP with MitoTracker and LysoTracker and performed fluorescence imaging (Fig. 5b). Free ICG and ICG-PFP had punctate localization around the nucleus. Colocalization studies with both MitoTracker and LysoTracker showed that ICG localizes into both mitochondria and lysosomes at varying degrees as has been previously reported by others [65, 66]. Moreover, the quantitative colocalization analysis indicated no significant difference (Table. S1) in organelle localization of the dyes in free form or when encapsulated in PFP nanodroplets (Fig. S4).

3. 5 BPD retains its phototoxicity in nanodroplets formulation

The dark toxicity of BPD-PFP nanodroplets is shown in Fig. S5a. Statistically significant cell death was observed with concentrations greater than 1 μM of BPD. Hence, to evaluate the phototoxicity of our nanodroplets we chose 0.25 μM concentration of BPD. The dark toxicity for all the PFP formulations is provided in Fig. S5b. The experiment timeline for the PDT study is provided in Fig. 6a. Empty PFP nanodroplets (Fig. 6b gray bars) had no toxicity. ICG-PFP (Fig. 6b green bar) did not cause any significant cell death at both the low or high light dose while BPD-PFP and BPD+ICG-PFP produced a dose dependent cell death (Fig. 6b red and dark blue bars respectively). Liposomal BPD, prepared similarly to Visudyne (the commercial product used in clinic), was compared to various nanodroplet formulations. No statistically significant difference was observed among BPD-PFP, liposomal BPD or BPD+ICG-PFP 1:1 group indicating BPD cytotoxic effect was not compromised when encapsulated within the PFP nanodroplets. However, there was significant difference in cytotoxic effect when ICG loading was higher in the nanodroplet formulation (BPD+ICG-PFP 1:2, Fig. 6b orange bars). The difference in the phototoxicity of BPD+ICG-PFP nanodroplets with different loading ratios could be due to the interference of ICG with the availability of photons for BPD excitation for photodynamic action. Alternatively, the singlet oxygen species generated by BPD post light irradiation could have led to photooxidation of the ICG as has been reported previously in solutions and tissue phantoms [48, 66-70] and ultimately reducing the singlet oxygen species available for cellular toxicity.

3. 6 *In vivo* tumor oxygenation measurements

The oxygen delivery ability of the nanodroplets was demonstrated in a murine model with subcutaneous head and neck tumor xenografts. The ultrasound images show the subcutaneous tumor (identified by green ROI in Fig. 7) as hypoechoic regions underneath the hyperechoic skin. The pre and post nanodroplets injection images were obtained at the same cross-section as evident in the ultrasound images. The corresponding oxygen saturation map of the tumor is shown in Fig. 7 with blue and red regions corresponding to the hypoxic and oxygenated regions, respectively. An overall increase in the oxygenation of the tumor can be observed in the images, as evident from the greater abundance of red pseudo colored regions (oxygenated) after the administration of the PFP nanodroplets. We performed pixel-wise quantification of the StO_2 in the tumor area and displayed the data as histogram in Fig. 8a. The histogram after PFP administration shifted towards the right and also increased in total pixel count above 60% StO_2. The average StO_2 in the PFP administered mice had significant increase in the overall tumor oxygenation content (Fig. 8b). In contrast, the total hemoglobin levels in the tumor showed no significant difference indicating no accumulation of endogenous absorbers during the study (Fig. 8c).

To further understand the relative increase of oxygen in different regions of the tumor post nanodroplets administration, we quantified StO_2 in multiple ROIs of area ~ 3.5 mm^2. The mean StO_2 of the tumors prior to nanodroplet administration was ~43%. Hence, we grouped the individual ROIs within the tumor based on pre-injection average StO_2 values. The areas in the tumor whose StO_2 was less than 43% in the pre-injection showed an increase in the StO_2, whereas the highly oxygenated areas (StO_2 > 43%) did not show an overall increase in the oxygenation (Fig. 8d & e). These results clearly indicate that our PFP nanodroplets are delivering oxygen to the hypoxic regions in the tumor. Finally, we validated the results of the StO_2 PA imaging with an oxygen sensor (Oxylite) placed in the tumor adjacent to the imaging plane. The oxygen sensor directly measures the oxygen in the vicinity of the sensor tip and does not reflect the overall tumor oxygenation increase. Overall, a 9.1 (± 1.8 S.E.M) fold increase in oxygen at the site of the sensor immediately after the administration and irradiation of the nanodroplets was observed proving that our nanodroplets supply oxygen to the hypoxic regions of the tumor that had an initial pO_2 values of < 10 mmHg (Fig. 8f).

We performed histological examination to demonstrate the PFP nanodroplets ability to deliver oxygen and relieve hypoxia in tumors. Figs. 8g-k show the IF images of the control and BPD+ICG-PFP 1:1 treated tumor

stained with DAPI for nuclei (blue), CD31 for vasculature (red) and pimonidazole for hypoxic regions (green). In the control tumor treated with only PBS (Fig. 8g), we can observe that pimonidazole signal (green) is more prevalent in the core of the tumor as expected. The zoomed insets clearly show the hypoxic areas present in regions away from the vasculature (Fig. 8h) as well around dysfunctional blood vessels (Fig. 8i). Post injection of the oxygenated nanodroplets, we observed a significant decrease in the tumor hypoxia. A representative IF image of a tumor injected with PFP droplets is shown in Fig. 8j. Very low pimonidazole signal can be seen here indicating a significant reduction in hypoxia. The core of the tumor region (Fig. 8k) had no pimonidazole signal, indicating our nanodroplets relieved hypoxia not only in non-functional vascular regions, but also to the core of the tumor. We quantified the IF images with a custom written MATLAB algorithm to calculate the pimonidazole positive areas and normalized with total tumor area. The quantification confirmed the qualitative observations that PFP nanodroplets can significantly reduce the hypoxic regions in the tumor (Fig. 8l).

In addition to the delivery of oxygen and BPD to the tumor, PFP nanodroplets are also good PA contrast agents due to ICG. The accumulation of PFP nanodroplets enhances the tumor contrast in PA imaging at 800 nm wavelength [47, 48]. The increase in PA signal post PFP nanodroplets administration can be clearly seen in Fig. S6 marked by the white arrows. Quantification of the different regions of the tumor showed a significant increase in the PA contrast due to ICG after the administration of PFP nanodroplets (Fig. 9a). PFC compounds are also used as contrast agents for ultrasonography [71-74]. PFP nanodroplets also increased the ultrasound contrast in the tumor as expected. The enhancement of ultrasound contrast is clearly visible in Fig. 7. Furthermore, quantification of the ultrasound intensity per total tumor area showed statistically significant increase (25%) post injection of nanodroplets (Fig. 9b).

3. 7 *In vivo* PDT efficacy of nanodroplets

Maximum ICG signal in the tumor occurred at 90 minutes post intravenous injection of the nanodroplets. (Fig. 10a). Hence, we chose a drug-light interval of 90 minutes for our *in vivo* PDT efficacy study. We also investigated the biodistribution of the nanodroplets 24 hours post intravenous administration. Quantification of ex vivo fluorescence images (Figs. 10b & c) showed that the tumor had higher uptake of nanodroplets than all the major excised organs except liver. To investigate the PDT efficacy with oxygen enriched nanodroplets, mice were divided into multiple treatment groups as shown in Figs. 11a & b. PFP nanodroplets (no BPD or ICG) did not produce any therapeutic

response as expected (Fig. 11b, gray line) and no statistically significant difference was observed between this group and the no-treatment control group (Fig. 11b, black line). ICG-PFP showed a moderate response to PDT at 690 nm irradiation (Fig. 11b, green line). Since ICG has a weak absorption at 690 nm, ICG could have been minimally excited and produced either a weak photothermal or PDT response at this wavelength [68, 75]. Data for ICG-PFP group was shown only up to day 12 as the mice had to be euthanized as per veterinarian recommendation. BPD-PFP group (Fig. 11a, red line) had better therapeutic response than the Visudyne (Fig. 11a, cyan line) because of its greater singlet oxygen production ability due to the extra oxygen present in the nanodroplets.

We evaluated the treatment efficacy of nanodroplets fabricated with different loading ratios of BPD and ICG. In Fig. 11b, we demonstrate that BPD+ICG-PFP with 1:2 BPD:ICG loading ratio (Fig. 11b, orange line) did not produce any therapeutic response as it was not statistically different from the no-treatment control group (Fig.11b, black line). This is in agreement with our *in vitro* data in Fig. 6 where the presence of higher ICG concentration in the nanodroplets significantly reduced the therapeutic efficacy of BPD. A possible mechanism could be the unavailability of photons for BPD's photodynamic action as ICG's molar extinction coefficient (36,483 $M^{-1}cm^{-1}$ in water [76] and ~35,000 $M^{-1}cm^{-1}$ in DMSO [48]) is approximately equal to BPD (34,895 $M^{-1}cm^{-1}$ in DMSO [48]) at 687 nm. Alternatively, the singlet oxygen species generated by BPD post light irradiation could have led to photooxidation of the ICG as has been reported previously in solutions and tissue phantoms [48, 66-70] and ultimately reduced singlet oxygen species available for cytotoxicity. BPD and ICG concentration in the BPD+ICG-PFP 1:1 (Fig. 11b, blue line) was optimized to retain the BPD's singlet oxygen production and ICG's PA signal response. BPD+ICG-PFP 1:1 (Fig. 11b, blue line) had a response similar to the BPD-PFP (Fig. 11a, red line) with no ICG (statistical information regarding the Fig. 11a & b are given in Tables S2 and S3). When incorporating multiple theranostic agents in a single carrier, it is important to optimize the loading concentration of different agents especially if they have similar optical absorption properties. The *in vivo* results for the BPD+ICG-PFP nanodroplets with different loading concentration complements the *in vitro* results obtained from our previous study [48]. In addition to investigating the efficacy of PFP nandroplets in reducing tumor volume, we examined the acute effects of the treatment (24 hours post treatment) in causing necrosis. The H&E image of a representative tumor cross-section in the control and BPD+ICG-PFP 1:1 group are shown in Figs. 11c & d. We can qualitatively envisage the necrosis imparted in the tumor by the oxygen loaded nanodroplets. The total necrotic area was quantified using a custom written MATLAB algorithm [77]. The tumors receiving BPD+ICG-PFP 1:1 with PDT treatment had ~50%

necrotic volume and was significantly greater than the control group (Fig. 10e). Overall, here we demonstrated that the nanodroplets presented in this study have multiple-theranostic properties, i.e., they enhance tumor ultrasound contrast, enhance photoacoustic contrast, and deliver oxygen and photosensitizer for superlative PDT performance compared to the clinical formulation Visudyne.

4. Conclusions

In this work, we successfully designed a new nanoconstruct, PFP nanodroplets loaded with photosensitizer, which can combat hypoxia by delivering oxygen and improve PDT efficacy. Furthermore, these multi-modal agents can not only deliver photosensitizer, but they can also be used to increase the contrast for photoacoustic and ultrasound imaging. We validated the ability of the nanodroplets to produce photoacoustic contrast, deliver oxygen, relieve hypoxia and improve PDT efficacy both *in vitro* and *in vivo*. In future studies, with aid of photoacoustic contrast provided by our engineered nanodroplets, we will explore the ability of nanodroplets to personalize PDT dose based on PS uptake, tumor vasculature and oxygenation content. Customizing PDT dose with these surrogate markers has previously shown to improve efficacy [7]. Our nanodroplets can also be used to increase oxygen content in other therapeutic strategies such as radiation and chemotherapy. Furthermore, these nanodroplets are made entirely from biocompatible and clinically approved materials that could potentially enable its transition to the clinic.

Conflicts of interest

There are no conflicts to declare.

Acknowledgements

The authors would like to gratefully acknowledge funds from the NIH S10OD026844 (Mallidi), R41CA221420 and R41EY028839 (Cook and Mallidi). The authors thank Dr. Tayyaba Hasan for access to VisualSonics Vevo LAZR system at Wellman Center for Photomedicine, Massachusetts General Hospital. Ms. Sophie Magidson for editing the manuscript for language, Drs. Girgis Obaid and Mohammad Saad at the Wellman Center for Photomedicine for their informative discussions on the experimental procedure, and Dr. Ryan Deschner and Mrs. Juili Kelvekar for their advice on the formulation.

Electronic Supplementary Material: Supplementary material (further details of the photoacoustic characterization, localization and dark toxicity of nanodroplets, biodistribution and photoacoustic contrast enhancement of nanodroplets) is available in the online version of this article at http://dx.doi.org/****.

Figure captions

Figure 1: a) Schematic depiction of the photoacoustic nanodroplets used for oxygen enhanced PDT. b) Size distribution of the nanodroplets obtained with a DLS system. c) Stability of PFP nanodroplets monitored over 6 weeks post synthesis. d-f) Normalized UV-Visible absorption spectra of nanodroplets compared to the free dyes (solid lines). The photoacoustic spectra of the various formulations of the nanodroplets in PBS shown in black dots.

Figure 2: a) PA images of the nanodroplets in a tube obtained at 800 nm wavelength irradiation. Scale bar = 1 mm. b) Time dependent change in PA signal of ICG-PFP or BPD+ICG-PFP nanodroplets in the tube over time. The data are normalized to the PA intensity at time t = 0 seconds. PA at 800 nm excite ICG to vaporize the droplets and release oxygen. c) Time dependent change in PA signal produced by BPD-PFP, ICG-PFP and BPD+ICG-PFP nanodroplets when irradiated at 690 nm.

Figure 3: a) Comparison of singlet oxygen production by free BPD and BPD-PFP in normal and hypoxic conditions at 0 and 20 J/cm^2 690 nm light irradiation. Analysis was performed using two-way ANOVA with Tukey's multiple comparison test: ** = $p < 0.01$ b) Singlet oxygen production of BPD+ICG-PFP with different ratios of BPD:ICG in the nanodroplets when irradiated with 690 nm wavelength. Analysis was performed using one-way ANOVA with a Tukey's multiple comparison test: * = $p < 0.05$, ** = $p < 0.01$ is performed. The results are expressed as mean ± S.E.M and each symbol denotes an experimental repeat.

Figure 4: Quantification of a) intracellular BPD and b) ICG concentrations with free PS and PFP nanodroplet formulations. The results are expressed as mean ± S.E.M and each symbol represents experimental replicate. Analysis was performed using one-way ANOVA with a Tukey's multiple comparison test: * = $p < 0.05$, **p = < 0.01.

Figure 5: a) Mitochondrial localization of free dye and nanodroplet formulations. BPD and ICG signals were pseudo-colored in red. MitoTracker (Green) was used to stain mitochondria. Scale bar = 20 µm. b) Lysosomal localization of free dye and nanodroplet formulations. LysoTracker (Green) was used to stain lysosomes. BPD and ICG signals were pseudo-colored in red. Nuclear staining was done with Hoechst (blue) on both the panels. Scale bar = 20 µm.

Figure 6: a) Experiment timeline for phototoxic studies with PFP nanodroplets. b) Dark toxicity of the nanodroplets

were subtracted from the light treated groups. BPD efficacy is largely not influenced by the presence of ICG except in the case of BPD+ICG-PFP 1:2 formulation. The results are expressed as mean ± S.E.M; Analysis was performed with two-way AVOVA with a Tukey's multiple comparison test: ** = $p < 0.01$, **** = $p < 0.0001$.

Figure 7: The ultrasound and photoacoustic oxygen saturation images of the tumor a) before and b) after injection of PFP nanodroplets where blue and red represents the hypoxic and oxygenated regions, respectively. The tumor region is identified with a green ROI and had ~ 9.1 (± 1.8 S.E.) fold increase in oxygen pO_2 (measured with oxygen sensor) and 25% increase in ultrasound contrast. Scale bar = 2 mm.

Figure 8: PFP nanodroplets enhance tumor oxygenation and reduce hypoxia in the tumors. Measurements performed before and after injection of nanodroplets ae shown in red and green color, respectively. a) Increase in StO2 histogram of a representative tumor shown in Fig. 7. b) Average StO_2 increase in the tumor after oxygen filled PFP nanodroplet administration. c) Total hemoglobin levels quantified from StO_2 imaging shows no significant change in the accumulation of endogenous absorbers. Regional analysis of StO_2 shows that PFP nanodroplets significantly enhanced oxygen in d) low StO_2 areas while e) high StO_2 regions maintained similar levels as before nandroplet administration. f) Validation of StO_2 imaging with oxygen sensor that was placed inside the tumor adjacent to the imaging plane. IF image of the tumor cross-section treated with g) control and treated with j) BPD+ICG-PFP 1:1 nanodroplets. The insets h, iand k show the tumor core at higher magnification with k) inset showing the core at higher magnification. l) Quantification of the hypoxic regions (ratio of pimonidazole positive area to total tumor area) from the IF image. The results are expressed as mean ± S.E.M; b, c, f, l – n=3 mice; d & e, multiple regions within the 3 tumors. Scale bar = 1 mm for g & j. *Scale bar* = 100 µm for h, i & k; b-f: paired two-tailed t test: * = $p < 0.05$, **** = $p < 0.0001$, l: unpaired two-tailed t test: *** = $p < 0.001$.

Figure 9: Measurements performed before and after injection of nanodroplets are shown in red and green color, respectively. a) PA contrast (800 nm wavelength) in the tumor increased post injection due to accumulation of the nanodroplets containing ICG. b) The tumor ultrasound contrast is also enhanced by the nanodroplets. The results are expressed as mean ± S.E.M; n = 3 mice; paired two-tailed t test: * = $p < 0.05$, **** = $p < 0.0001$.

Figure 10: a) *In vivo* pharmacokinetics of nanodroplets. ICG fluorescence in the tumor following the administration of BPD+ICG-PFP nanodroplets was monitored at different time points. The results are expressed as mean ± S.E.M (n=3). b) Representative fluorescence image of excised organs 24 hours post administration of BPD+ICG-PFP nanodroplets. c) Average fluorescence intensity in various excised organs demonstrating the biodistribution of the nanodroplets *in vivo*. The results are expressed as mean ± S.E.M; n=3 mice in each group.

Figure 11: Change in tumor volume in response to PDT treatment with nanodroplet variants. a) Oxygen enhanced BPD-PFP (red line) is significantly efficacious than the clinically used formulation of BPD i.e., Visudyne (cyan line). The tumor volume in the no-treatment group are shown in black line. ICG-PFP nanodroplets had minimal therapeutic effect. b) The tumor volume of the mice in the PFP only group are shown in gray line. The ratio of

BPD:ICG ratio within the nanodroplets is critical to achieve effective therapeutic outcome. BPD:ICG 1:1 formulation (blue line) had better efficacy than the BPD:ICG 1:2 formulation (orange line). The H&E image of the tumors in c) non-treated group and d) 24 hours post PDT with BPD+ICG-PFP 1:1 nanodroplets group. The insets show the tumor core at higher magnification. Scale bar in the inset = 1 mm. e) Quantification of necrotic regions in the tumors show higher values in the PDT with BPD+ICG-PFP 1:1 nanodroplets group compared to the control group. The results are expressed as mean ± S.E.M; n = 3-4 mice per group ; Two-way ANOVA with Tukey's multiple comparison test: * = $p < 0.05$.

References

[1] J.P. Celli, B.Q. Spring, I. Rizvi, C.L. Evans, K.S. Samkoe, S. Verma, B.W. Pogue, T. Hasan, Imaging and photodynamic therapy: mechanisms, monitoring, and optimization, Chem Rev 110(5) (2010) 2795-838.

[2] S. Mallidi, B.Q. Spring, S. Chang, B. Vakoc, T. Hasan, Optical Imaging, Photodynamic Therapy and Optically Triggered Combination Treatments, Cancer J 21(3) (2015) 194-205.

[3] R.M.A. Al-Delayme, H. Radhi, A. Farag, T. Al-Allaq, P. Virdee, R. Almudamgha, M. Al-Hadad, A. Fashid, A.F. Alani, M. Awda, Z. Alnajar, S.A.I. Alsamaraie, S. Elnashef, H. Mohammed, A. Yassin, Photodynamic Therapy as a Treatment Option for Oral Cancer and Dysplasia, Ann Med Health Sci R 8 (2018) 59-64.

[4] W. Jerjes, T. Upile, Z. Hamdoon, C. Alexander Mosse, M. Morcos, C. Hopper, Photodynamic therapy outcome for T1/T2 N0 oral squamous cell carcinoma, Lasers Surg Med 43(6) (2011) 463-9.

[5] N. Rigual, G. Shafirstein, M.T. Cooper, H. Baumann, D.A. Bellnier, U. Sunar, E.C. Tracy, D.J. Rohrbach, G. Wilding, W. Tan, M. Sullivan, M. Merzianu, B.W. Henderson, Photodynamic therapy with 3-(1'-hexyloxyethyl) pyropheophorbide a for cancer of the oral cavity, Clin Cancer Res 19(23) (2013) 6605-13.

[6] S. Mallidi, A.P. Khan, H. Liu, L. Daly, G. Rudd, P. Leon, S. Khan, B.M.A. Hussain, S.A. Hasan, S.A. Siddique, K. Akhtar, M. August, M. Troulis, F. Cuckov, J.P. Celli, T. Hasan, Platform for ergonomic intraoral photodynamic therapy using low-cost, modular 3D-printed components: Design, comfort and clinical evaluation, Sci Rep 9(1) (2019) 15830.

[7] B.C. Wilson, M.S. Patterson, L. Lilge, Implicit and explicit dosimetry in photodynamic therapy: a New paradigm, Lasers Med Sci 12(3) (1997) 182-99.

[8] L. Cincotta, D. Szeto, E. Lampros, T. Hasan, A.H. Cincotta, Benzophenothiazine and benzoporphyrin derivative combination phototherapy effectively eradicates large murine sarcomas, Photochem Photobiol 63(2) (1996) 229-37.

[9] J.M. Brown, W.R. Wilson, Exploiting tumour hypoxia in cancer treatment, Nat Rev Cancer 4(6) (2004) 437-47.

[10] K. Graham, E. Unger, Overcoming tumor hypoxia as a barrier to radiotherapy, chemotherapy and immunotherapy in cancer treatment, Int J Nanomedicine 13 (2018) 6049-6058.

[11] P. Vaupel, A. Mayer, Hypoxia in cancer: significance and impact on clinical outcome, Cancer Metastasis Rev 26(2) (2007) 225-39.

[12] M. Hockel, P. Vaupel, Tumor hypoxia: definitions and current clinical, biologic, and molecular aspects, J Natl Cancer Inst 93(4) (2001) 266-76.

[13] F. Tomaselli, A. Maier, H. Pinter, H. Stranzl, F.M. Smolle-Juttner, Photodynamic therapy enhanced by hyperbaric oxygen in acute endoluminal palliation of malignant bronchial stenosis (clinical pilot study in 40 patients), Eur J Cardiothorac Surg 19(5) (2001) 549-54.

[14] A. Maier, U. Anegg, B. Fell, P. Rehak, B. Ratzenhofer, F. Tomaselli, O. Sankin, H. Pinter, F.M. Smolle-Juttner, G.B. Friehs, Hyperbaric oxygen and photodynamic therapy in the treatment of advanced carcinoma of the cardia and the esophagus, Lasers Surg Med 26(3)

(2000) 308-15.
[15] A. Maier, U. Anegg, F. Tomaselli, P. Rehak, O. Sankin, B. Fell, H. Renner, H. Pinter, F.M. Smolle-Juttner, G.B. Friehs, Does hyperbaric oxygen enhance the effect of photodynamic therapy in patients with advanced esophageal carcinoma? A clinical pilot study, Endoscopy 32(1) (2000) 42-48.
[16] J.M. Clark, C.J. Lambertsen, Pulmonary oxygen toxicity: a review, Pharmacol Rev 23(2) (1971) 37-133.
[17] S.R. Thom, Hyperbaric oxygen: its mechanisms and efficacy, Plast Reconstr Surg 127 Suppl 1 (2011) 131S-141S.
[18] M. Heyboer, 3rd, D. Sharma, W. Santiago, N. McCulloch, Hyperbaric Oxygen Therapy: Side Effects Defined and Quantified, Adv Wound Care (New Rochelle) 6(6) (2017) 210-224.
[19] Y. Sheng, H. Nesbitt, B. Callan, M.A. Taylor, M. Love, A.P. McHale, J.F. Callan, Oxygen generating nanoparticles for improved photodynamic therapy of hypoxic tumours, J Control Release 264 (2017) 333-340.
[20] S. Gao, G. Wang, Z. Qin, X. Wang, G. Zhao, Q. Ma, L. Zhu, Oxygen-generating hybrid nanoparticles to enhance fluorescent/photoacoustic/ultrasound imaging guided tumor photodynamic therapy, Biomaterials 112 (2017) 324-335.
[21] J.J. Kwan, M. Kaya, M.A. Borden, P.A. Dayton, Theranostic oxygen delivery using ultrasound and microbubbles, Theranostics 2(12) (2012) 1174-1184.
[22] J.R. Eisenbrey, R. Shraim, J.-B. Liu, J. Li, M. Stanczak, B. Oeffinger, D.B. Leeper, S.W. Keith, L.J. Jablonowski, F. Forsberg, P. O'Kane, M.A. Wheatley, Sensitization of Hypoxic Tumors to Radiation Therapy Using Ultrasound-Sensitive Oxygen Microbubbles, International Journal of Radiation Oncology*Biology*Physics 101(1) (2018) 88-96.
[23] L. Duan, L. Yang, J. Jin, F. Yang, D. Liu, K. Hu, Q. Wang, Y. Yue, N. Gu, Micro/nano-bubble-assisted ultrasound to enhance the EPR effect and potential theranostic applications, Theranostics 10(2) (2020) 462-483.
[24] M.S. Khan, J. Hwang, K. Lee, Y. Choi, K. Kim, H.-J. Koo, J.W. Hong, J. Choi, Oxygen-Carrying Micro/Nanobubbles: Composition, Synthesis Techniques and Potential Prospects in Photo-Triggered Theranostics, Molecules 23(9) (2018).
[25] S.M. Fix, V. Papadopoulou, H. Velds, S.K. Kasoji, J.N. Rivera, M.A. Borden, S. Chang, P.A. Dayton, Oxygen microbubbles improve radiotherapy tumor control in a rat fibrosarcoma model – A preliminary study, PLOS ONE 13(4) (2018) e0195667.
[26] A.L.Y. Kee, B.M. Teo, Biomedical applications of acoustically responsive phase shift nanodroplets: Current status and future directions, Ultrasonics Sonochemistry 56 (2019) 37-45.
[27] Y.-Z. Zhao, L.-N. Du, C.-T. Lu, Y.-G. Jin, S.-P. Ge, Potential and problems in ultrasound-responsive drug delivery systems, Int J Nanomedicine 8 (2013) 1621-1633.
[28] M. Kuriakose, M.A. Borden, Microbubbles and Nanodrops for photoacoustic tomography, Current Opinion in Colloid & Interface Science 55 (2021) 101464.
[29] X. Tang, Y. Cheng, S. Huang, F. Zhi, A. Yuan, Y. Hu, J. Wu, Overcome the limitation of hypoxia against photodynamic therapy to treat cancer cells by using perfluorocarbon nanodroplet for photosensitizer delivery, Biochem Biophys Res Commun 487(3) (2017) 483-487.
[30] Y. Cheng, H. Cheng, C. Jiang, X. Qiu, K. Wang, W. Huan, A. Yuan, J. Wu, Y. Hu, Perfluorocarbon nanoparticles enhance reactive oxygen levels and tumour growth inhibition in photodynamic therapy, Nat Commun 6 (2015) 8785.
[31] Y. Xiang, N. Bernards, B. Hoang, J. Zheng, N. Matsuura, Perfluorocarbon nanodroplets can reoxygenate hypoxic tumors in vivo without carbogen breathing, Nanotheranostics 3(2) (2019) 135-144.
[32] C.I. Castro, J.C. Briceno, Perfluorocarbon-Based Oxygen Carriers: Review of Products and Trials, Artificial Organs 34(8) (2010) 622-634.
[33] A.M.A. Dias, M. Freire, J.A.P. Coutinho, I.M. Marrucho, Solubility of oxygen in liquid perfluorocarbons1Paper Presented at the 15th Symposium on Thermophysical Properties, June 22–27, 2003, Boulder, CO, USA.1, Fluid Phase Equilibria 222-223 (2004) 325-330.
[34] A. Hannah, G. Luke, K. Wilson, K. Homan, S. Emelianov, Indocyanine green-loaded photoacoustic nanodroplets: dual contrast

nanoconstructs for enhanced photoacoustic and ultrasound imaging, ACS Nano 8(1) (2014) 250-9.

[35] M.P. Krafft, Fluorocarbons and fluorinated amphiphiles in drug delivery and biomedical research, Adv Drug Deliv Rev 47(2-3) (2001) 209-28.

[36] A. Scheer, M. Kirsch, K.B. Ferenz, perfluorocarbons in photodynamic and photothermal therapy, J Nanosci Nanomed 1 (2017) 21-27.

[37] K. Loskutova, D. Grishenkov, M. Ghorbani, Review on Acoustic Droplet Vaporization in Ultrasound Diagnostics and Therapeutics, Biomed Res Int 2019 (2019) 9480193.

[38] H. Hu, X. Yan, H. Wang, J. Tanaka, M. Wang, W. You, Z. Li, Perfluorocarbon-based O2 nanocarrier for efficient photodynamic therapy, J Mater Chem B 7(7) (2019) 1116-1123.

[39] Z. Wang, X. Gong, J. Li, H. Wang, X. Xu, Y. Li, X. Sha, Z. Zhang, Oxygen-Delivering Polyfluorocarbon Nanovehicles Improve Tumor Oxygenation and Potentiate Photodynamic-Mediated Antitumor Immunity, ACS Nano (2021).

[40] M. Funovics, R. Weissleder, C.H. Tung, Protease sensors for bioimaging, Anal Bioanal Chem 377(6) (2003) 956-63.

[41] G. Kim, S.W. Huang, K.C. Day, M. O'Donnell, R.R. Agayan, M.A. Day, R. Kopelman, S. Ashkenazi, Indocyanine-green-embedded PEBBLEs as a contrast agent for photoacoustic imaging, J Biomed Opt 12(4) (2007) 044020.

[42] R. Bam, M. Laffey, K. Nottberg, P.S. Lown, B.J. Hackel, K.E. Wilson, Affibody-Indocyanine Green Based Contrast Agent for Photoacoustic and Fluorescence Molecular Imaging of B7-H3 Expression in Breast Cancer, Bioconjug Chem 30(6) (2019) 1677-1689.

[43] C.-P. Spatarelu, A. Van Namen, G.P. Luke, Optically Activatable Double-Drug-Loaded Perfluorocarbon Nanodroplets for On-Demand Image-Guided Drug Delivery, ACS Applied Nano Materials 4(8) (2021) 8026-8038.

[44] D. Sheng, L. Deng, P. Li, Z. Wang, Q. Zhang, Perfluorocarbon Nanodroplets with Deep Tumor Penetration and Controlled Drug Delivery for Ultrasound/Fluorescence Imaging Guided Breast Cancer Therapy, ACS Biomater Sci Eng 7(2) (2021) 605-616.

[45] M. Xu, L.V. Wang, Photoacoustic imaging in biomedicine, Review of Scientific Instruments 77(4) (2006).

[46] S. Mallidi, K. Watanabe, D. Timerman, D. Schoenfeld, T. Hasan, Prediction of Tumor Recurrence and Therapy Monitoring Using Ultrasound-Guided Photoacoustic Imaging, Theranostics 5(3) (2015) 289-301.

[47] S. Mallidi, G.P. Luke, S. Emelianov, Photoacoustic imaging in cancer detection, diagnosis, and treatment guidance, Trends Biotechnol 29(5) (2011) 213-21.

[48] L.Z. Petrovic, M. Xavierselvan, M. Kuriakose, M.D. Kennedy, C.D. Nguyen, J.J. Batt, K.B. Detels, S. Mallidi, Mutual impact of clinically translatable near-infrared dyes on photoacoustic image contrast and in vitro photodynamic therapy efficacy, J Biomed Opt 25(6) (2020) 1-12.

[49] G. Obaid, S. Bano, S. Mallidi, M. Broekgaarden, J. Kuriakose, Z. Silber, A.L. Bulin, Y. Wang, Z. Mai, W. Jin, D. Simeone, T. Hasan, Impacting Pancreatic Cancer Therapy in Heterotypic in Vitro Organoids and in Vivo Tumors with Specificity-Tuned, NIR-Activable Photoimmunonanoconjugates: Towards Conquering Desmoplasia?, Nano Lett 19(11) (2019) 7573-7587.

[50] N.Y. Rapoport, A.M. Kennedy, J.E. Shea, C.L. Scaife, K.H. Nam, Controlled and targeted tumor chemotherapy by ultrasound-activated nanoemulsions/microbubbles, J Control Release 138(3) (2009) 268-76.

[51] N.Y. Rapoport, A.L. Efros, D.A. Christensen, A.M. Kennedy, K.-H. Nam, Microbubble Generation in Phase-Shift Nanoemulsions used as Anticancer Drug Carriers, Bubble Sci Eng Technol 1(1-2) (2009) 31-39.

[52] E.J. Barber, G.H. Cady, Vapor Pressures of Perfluoropentanes, J Phys Chem-Us 60(4) (1956) 504-505.

[53] I. Rizvi, S. Nath, G. Obaid, M.K. Ruhi, K. Moore, S. Bano, D. Kessel, T. Hasan, A Combination of Visudyne and a Lipid-anchored Liposomal Formulation of Benzoporphyrin Derivative Enhances Photodynamic Therapy Efficacy in a 3D Model for Ovarian Cancer, Photochem Photobiol 95(1) (2019) 419-429.

[54] S. Anbil, I. Rizvi, J.P. Celli, N. Alagic, B.W. Pogue, T. Hasan, Impact of treatment response metrics on photodynamic therapy planning and outcomes in a three-dimensional model of ovarian cancer, Journal of biomedical optics 18(9) (2013) 098004-098004.

[55] M.W. Dewhirst, T.W. Secomb, Transport of drugs from blood vessels to tumour tissue, Nat Rev Cancer 17(12) (2017) 738-750.
[56] R.K. Jain, Transport of molecules across tumor vasculature, Cancer and Metastasis Reviews 6(4) (1987) 559-593.
[57] L.Y. Chou, K. Ming, W.C. Chan, Strategies for the intracellular delivery of nanoparticles, Chem Soc Rev 40(1) (2011) 233-45.
[58] M. Mahmoudi, J. Meng, X. Xue, X.J. Liang, M. Rahman, C. Pfeiffer, R. Hartmann, P.R. Gil, B. Pelaz, W.J. Parak, P. Del Pino, S. Carregal-Romero, A.G. Kanaras, S. Tamil Selvan, Interaction of stable colloidal nanoparticles with cellular membranes, Biotechnol Adv 32(4) (2014) 679-92.
[59] B. Yameen, W.I. Choi, C. Vilos, A. Swami, J. Shi, O.C. Farokhzad, Insight into nanoparticle cellular uptake and intracellular targeting, J Control Release 190 (2014) 485-499.
[60] P. Foroozandeh, A.A. Aziz, Insight into Cellular Uptake and Intracellular Trafficking of Nanoparticles, Nanoscale Res Lett 13(1) (2018) 339.
[61] N. Onda, M. Kimura, T. Yoshida, M. Shibutani, Preferential tumor cellular uptake and retention of indocyanine green for in vivo tumor imaging, Int J Cancer 139(3) (2016) 673-82.
[62] C.D. Chan, M.J. Brookes, R. Tanwani, C. Hope, T.A. Pringle, J.C. Knight, K.S. Rankin, Investigating the mechanisms of indocyanine green (ICG) cellular uptake in sarcoma, bioRxiv (2021) 2021.04.05.438013.
[63] D. Kessel, Y. Luo, Mitochondrial photodamage and PDT-induced apoptosis, J Photochem Photobiol B 42(2) (1998) 89-95.
[64] I. Rizvi, G. Obaid, S. Bano, T. Hasan, D. Kessel, Photodynamic therapy: Promoting in vitro efficacy of photodynamic therapy by liposomal formulations of a photosensitizing agent, Lasers Surg Med 50(5) (2018) 499-505.
[65] N. Onda, R. Mizutani-Morita, S. Yamashita, R. Nagahara, S. Matsumoto, T. Yoshida, M. Shibutani, Fluorescence contrast-enhanced proliferative lesion imaging by enema administration of indocyanine green in a rat model of colon carcinogenesis, Oncotarget 8(52) (2017) 90278-90290.
[66] C. Abels, S. Fickweiler, P. Weiderer, W. Baumler, F. Hofstadter, M. Landthaler, R.M. Szeimies, Indocyanine green (ICG) and laser irradiation induce photooxidation, Arch Dermatol Res 292(8) (2000) 404-11.
[67] G. Camille, M. Albert, S. Aurelie, M. Serge, F. Celine, Indocyanine Green: Photosensitizer or Chromophore? Still a Debate, Current Medicinal Chemistry 21(16) (2014) 1871-1897.
[68] S. Reindl, A. Penzkofer, S.H. Gong, M. Landthaler, R.M. Szeimies, C. Abels, W. Bäumler, Quantum yield of triplet formation for indocyanine green, Journal of Photochemistry and Photobiology A: Chemistry 105(1) (1997) 65-68.
[69] W. Holzer, M. Mauerer, A. Penzkofer, R.M. Szeimies, C. Abels, M. Landthaler, W. Bäumler, Photostability and thermal stability of indocyanine green, Journal of Photochemistry and Photobiology B: Biology 47(2) (1998) 155-164.
[70] F.M. Penha, E.B. Rodrigues, M. Maia, C.H. Meyer, E. de Paula Fiod Costa, E. Dib, E. Bechara, A. Lourenço, A.A.S. Lima Filho, E.H. Freymüller, M.E. Farah, Biochemical Analysis and Decomposition Products of Indocyanine Green in Relation to Solvents, Dye Concentrations and Laser Exposure, Ophthalmologica 230(suppl 2)(Suppl. 2) (2013) 59-67.
[71] P.S. Sheeran, P.A. Dayton, Phase-change contrast agents for imaging and therapy, Curr Pharm Des 18(15) (2012) 2152-65.
[72] N. Reznik, R. Williams, P.N. Burns, Investigation of Vaporized Submicron Perfluorocarbon Droplets as an Ultrasound Contrast Agent, Ultrasound in Medicine & Biology 37(8) (2011) 1271-1279.
[73] N. Deshpande, A. Needles, J.K. Willmann, Molecular ultrasound imaging: current status and future directions, Clinical Radiology 65(7) (2010) 567-581.
[74] D.Y. Santiesteban, K.A. Hallam, S.K. Yarmoska, S.Y. Emelianov, Color-coded perfluorocarbon nanodroplets for multiplexed ultrasound and Photoacoustic imaging, Nano Res 12(4) (2019) 741-747.
[75] J. Atchison, S. Kamila, H. Nesbitt, K.A. Logan, D.M. Nicholas, C. Fowley, J. Davis, B. Callan, A.P. McHale, J.F. Callan, Iodinated cyanine dyes: a new class of sensitisers for use in NIR activated photodynamic therapy (PDT), Chemical Communications 53(12) (2017) 2009-2012.
[76] M.L. Landsman, G. Kwant, G.A. Mook, W.G. Zijlstra, Light-absorbing properties, stability, and spectral stabilization of

indocyanine green, Journal of Applied Physiology 40(4) (1976) 575-583.

[77] S. Mallidi, S. Anbil, S. Lee, D. Manstein, S. Elrington, G. Kositratna, D. Schoenfeld, B. Pogue, S.J. Davis, T. Hasan, Photosensitizer fluorescence and singlet oxygen luminescence as dosimetric predictors of topical 5-aminolevulinic acid photodynamic therapy induced clinical erythema, J Biomed Opt 19(2) (2014) 028001.

Figures

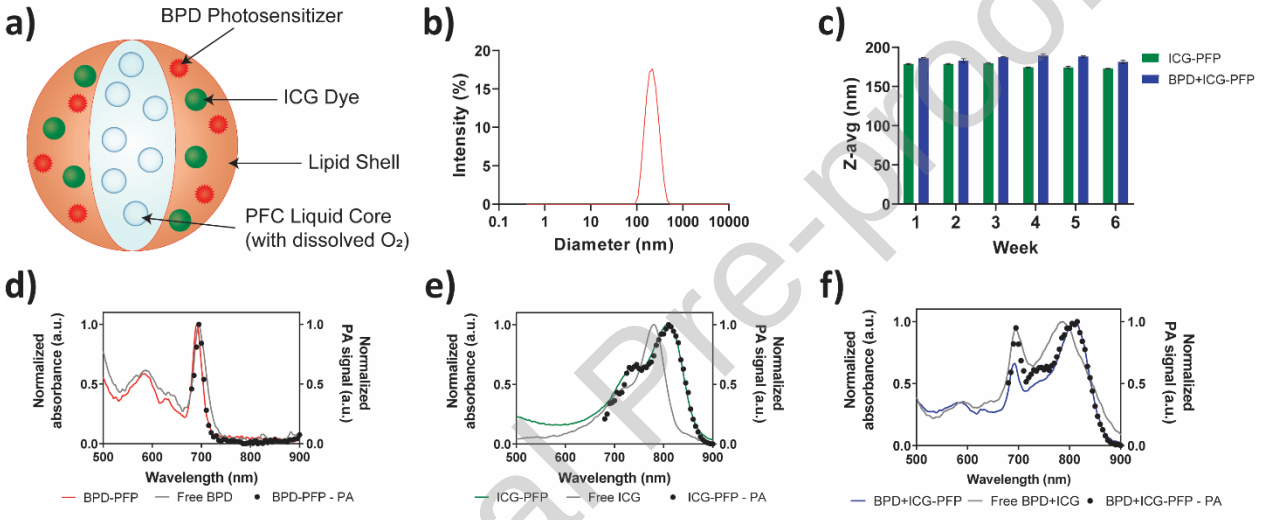

Figure 1: a) Schematic depiction of the photoacoustic nanodroplets used for oxygen enhanced PDT. b) Size distribution of the nanodroplets obtained with a DLS system. c) Stability of PFP nanodroplets monitored over 6 weeks post synthesis. d-f) Normalized UV-Visible absorption spectra of nanodroplets compared to the free dyes (solid lines). The photoacoustic spectra of the various formulations of the nanodroplets in PBS shown in black dots.

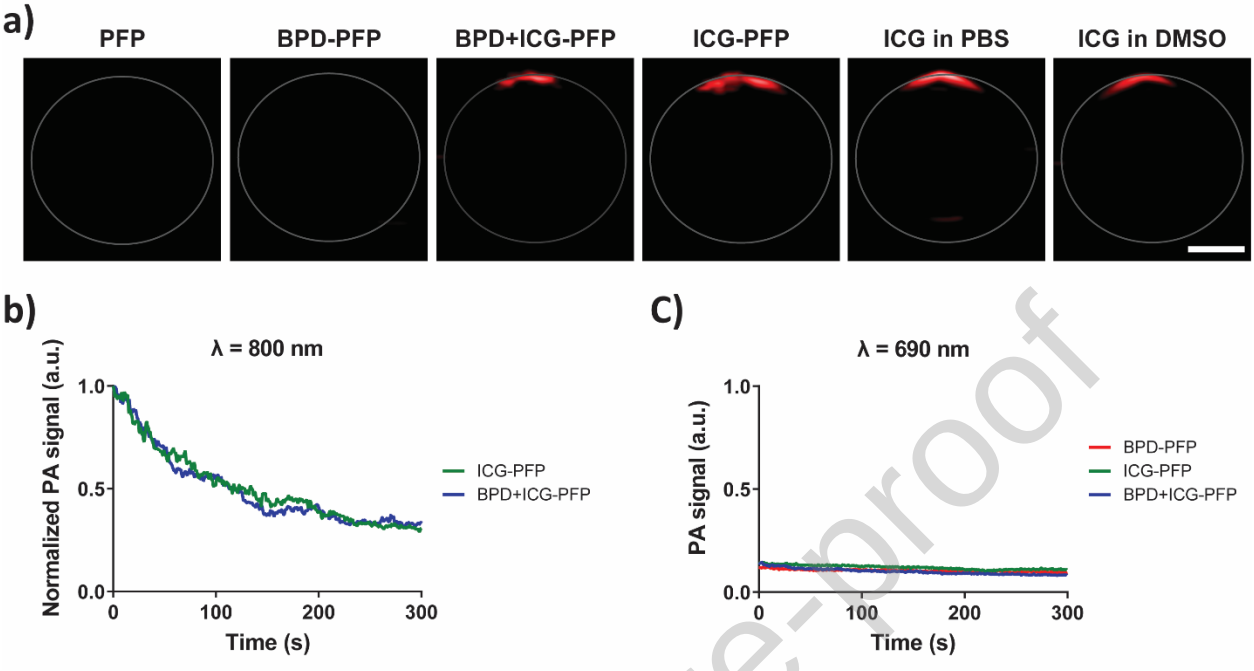

Figure 2: a) PA images of the nanodroplets in a tube obtained at 800 nm wavelength irradiation. Scale bar = 1 mm. b) Time dependent change in PA signal of ICG-PFP or BPD+ICG-PFP nanodroplets in the tube over time. The data are normalized to the PA intensity at time t = 0 seconds. PA at 800 nm excite ICG to vaporize the droplets and release oxygen. c) Time dependent change in PA signal produced by BPD-PFP, ICG-PFP and BPD+ICG-PFP nanodroplets when irradiated at 690 nm.

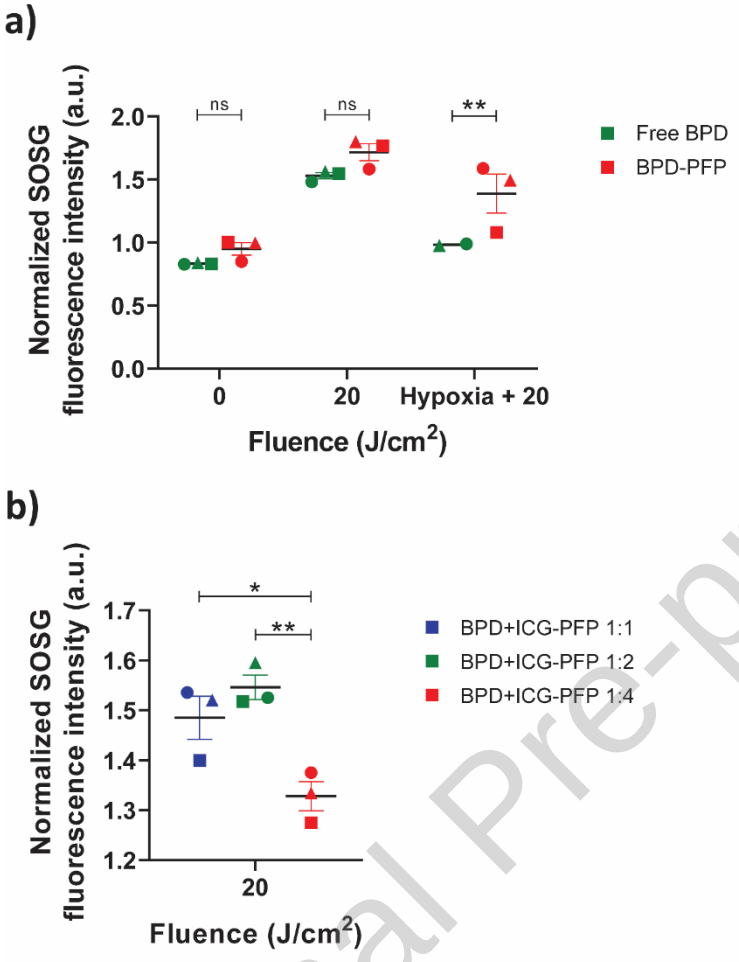

Figure 3: a) Comparison of singlet oxygen production by free BPD and BPD-PFP in normal and hypoxic conditions at 0 and 20 J/cm^2 690 nm light irradiation. Analysis was performed using two-way ANOVA with Tukey's multiple comparison test: ** = $p < 0.01$ b) Singlet oxygen production of BPD+ICG-PFP with different ratios of BPD:ICG in the nanodroplets when irradiated with 690 nm wavelength. Analysis was performed using one-way ANOVA with a Tukey's multiple comparison test: * = $p < 0.05$, ** = $p < 0.01$ is performed. The results are expressed as mean ± S.E.M and each symbol denotes an experimental repeat.

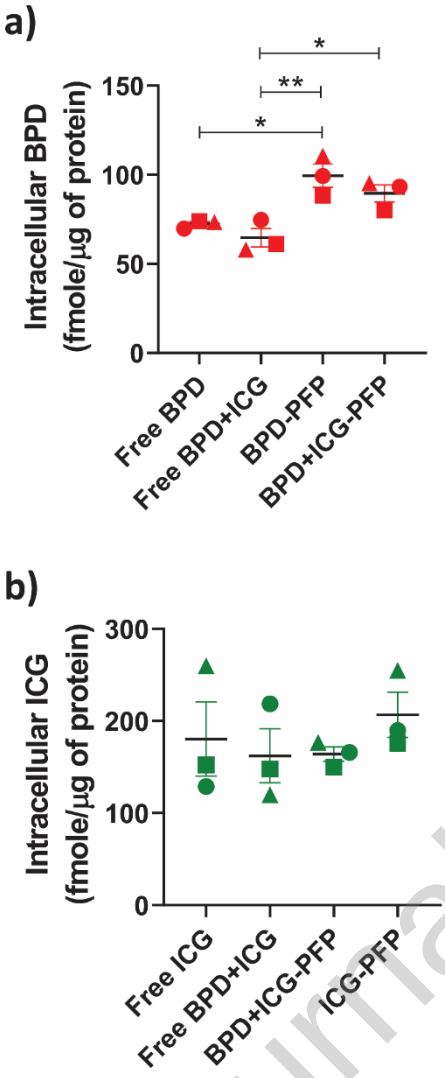

Figure 4: Quantification of a) intracellular BPD and b) ICG concentrations with free PS and PFP nanodroplet formulations. The results are expressed as mean ± S.E.M and each symbol represents experimental replicate. Analysis was performed using one-way ANOVA with a Tukey's multiple comparison test: * = $p < 0.05$, **p = < 0.01.

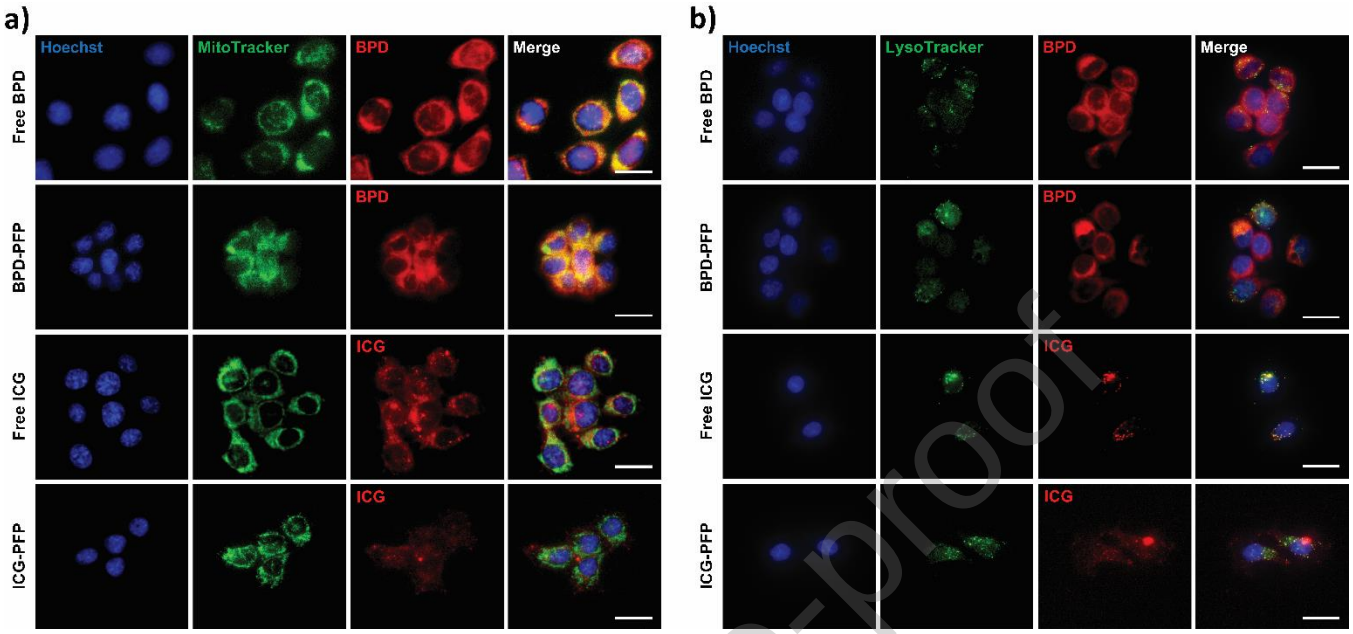

Figure 5: a) Mitochondrial localization of free dye and nanodroplet formulations. BPD and ICG signals were pseudo-colored in red. MitoTracker (Green) was used to stain mitochondria. Scale bar = 20 µm. b) Lysosomal localization of free dye and nanodroplet formulations. LysoTracker (Green) was used to stain lysosomes. BPD and ICG signals were pseudo-colored in red. Nuclear staining was done with Hoechst (blue) on both the panels. Scale bar = 20 µm.

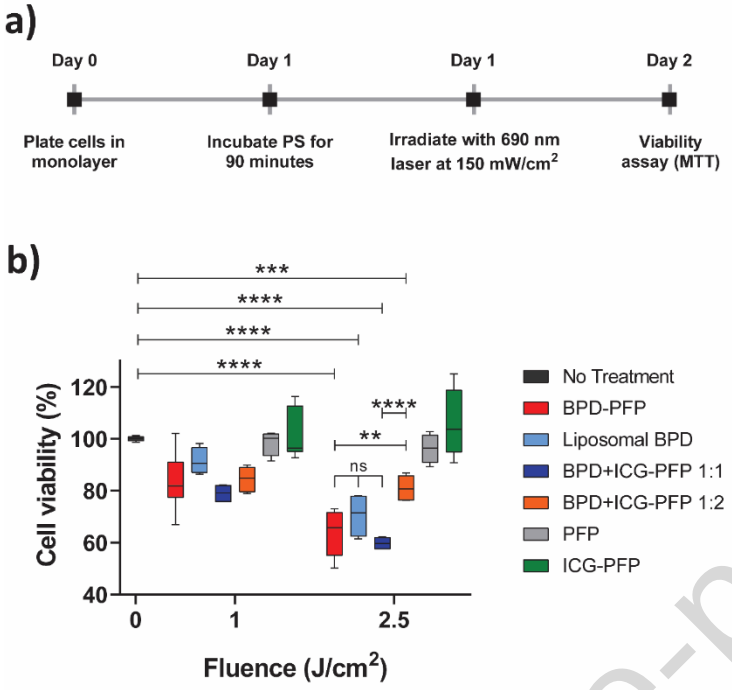

Figure 6: a) Experiment timeline for phototoxic studies with PFP nanodroplets. b) Dark toxicity of the nanodroplets were subtracted from the light treated groups. BPD efficacy is largely not influenced by the presence of ICG except in the case of BPD+ICG-PFP 1:2 formulation. The results are expressed as mean ± S.E.M; Analysis was performed with two-way AVOVA with a Tukey's multiple comparison test: ** = $p < 0.01$, **** = $p < 0.0001$.

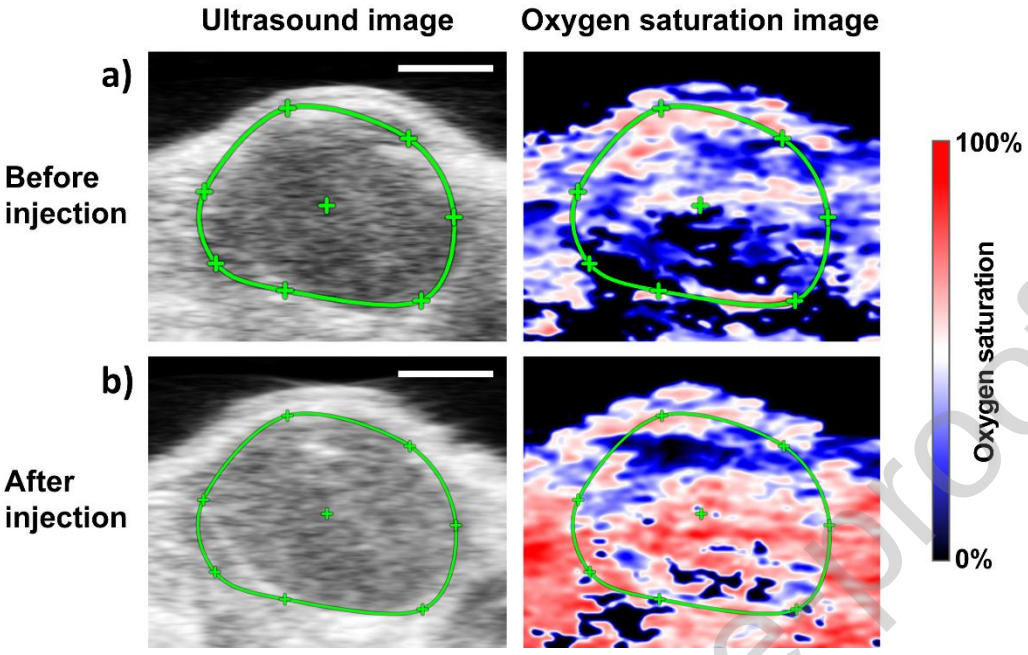

Figure 7: The ultrasound and photoacoustic oxygen saturation images of the tumor a) before and b) after injection of PFP nanodroplets where blue and red represents the hypoxic and oxygenated regions, respectively. The tumor region is identified with a green ROI and had ~ 9.1 (± 1.8 S.E.) fold increase in oxygen pO_2 (measured with oxygen sensor) and 25% increase in ultrasound contrast. Scale bar = 2 mm.

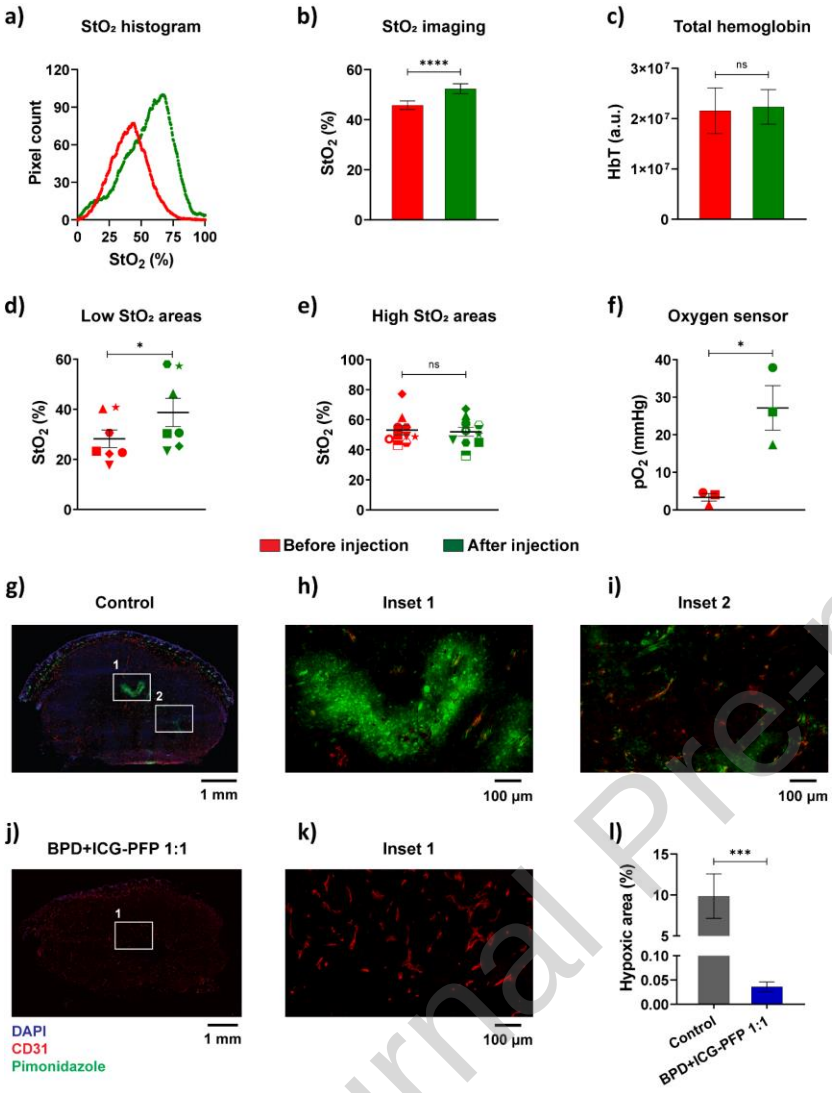

Figure 8: PFP nanodroplets enhance tumor oxygenation and reduce hypoxia in the tumors. Measurements performed before and after injection of nanodroplets ae shown in red and green color, respectively. a) Increase in StO2 histogram of a representative tumor shown in Fig. 7. b) Average StO_2 increase in the tumor after oxygen filled PFP nanodroplet administration. c) Total hemoglobin levels quantified from StO_2 imaging shows no significant change in the accumulation of endogenous absorbers. Regional analysis of StO_2 shows that PFP nanodroplets significantly enhanced oxygen in d) low StO_2 areas while e) high StO_2 regions maintained similar levels as before nandroplet administration. f) Validation of StO_2 imaging with oxygen sensor that was placed inside the tumor adjacent to the imaging plane. IF image of the tumor cross-section treated with g) control and treated with j) BPD+ICG-PFP 1:1 nanodroplets. The insets h, iand k show the tumor core at higher magnification with k) inset showing the core at higher magnification. l) Quantification of the hypoxic regions (ratio of pimonidazole positive area to total tumor area) from the IF image. The results are expressed as mean ± S.E.M; b, c, f, l – n=3 mice; d & e, multiple regions within the 3 tumors. Scale bar = 1 mm for g & j. *Scale bar* = 100 µm for h, i & k; b-f: paired two-tailed t test: * = $p < 0.05$, **** = $p < 0.0001$, l: unpaired two-tailed t test: *** = $p < 0.001$.

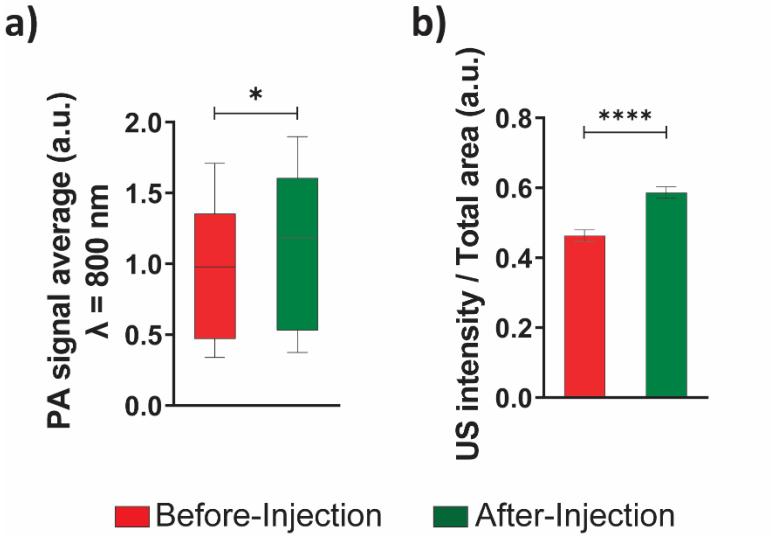

Figure 9: Measurements performed before and after injection of nanodroplets are shown in red and green color, respectively. a) PA contrast (800 nm wavelength) in the tumor increased post injection due to accumulation of the nanodroplets containing ICG. b) The tumor ultrasound contrast is also enhanced by the nanodroplets. The results are expressed as mean ± S.E.M; n = 3 mice; paired two-tailed t test: * = $p < 0.05$, **** = $p < 0.0001$.

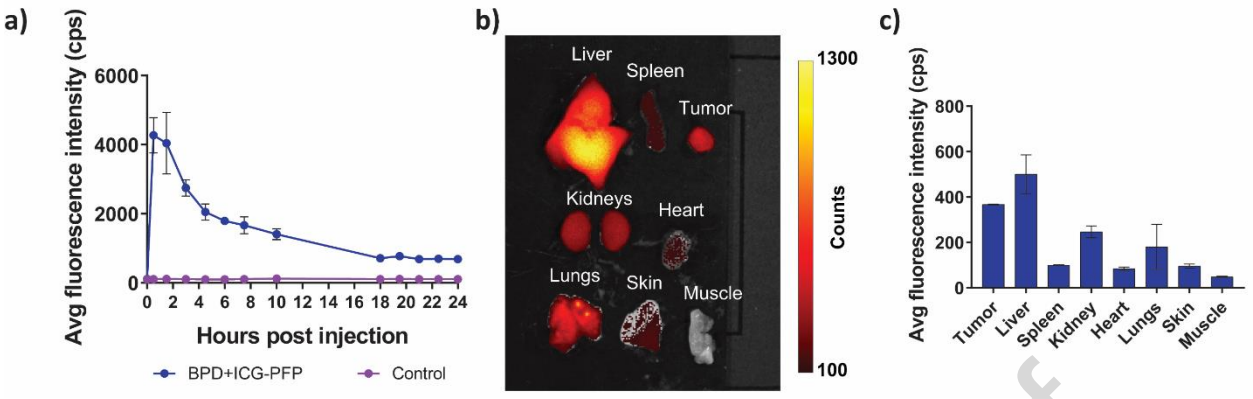

Figure 10: a) *In vivo* pharmacokinetics of nanodroplets. ICG fluorescence in the tumor following the administration of BPD+ICG-PFP nanodroplets was monitored at different time points. The results are expressed as mean ± S.E.M (n=3). b) Representative fluorescence image of excised organs 24 hours post administration of BPD+ICG-PFP nanodroplets. c) Average fluorescence intensity in various excised organs demonstrating the biodistribution of the nanodroplets *in vivo*. The results are expressed as mean ± S.E.M; n=3 mice in each group.

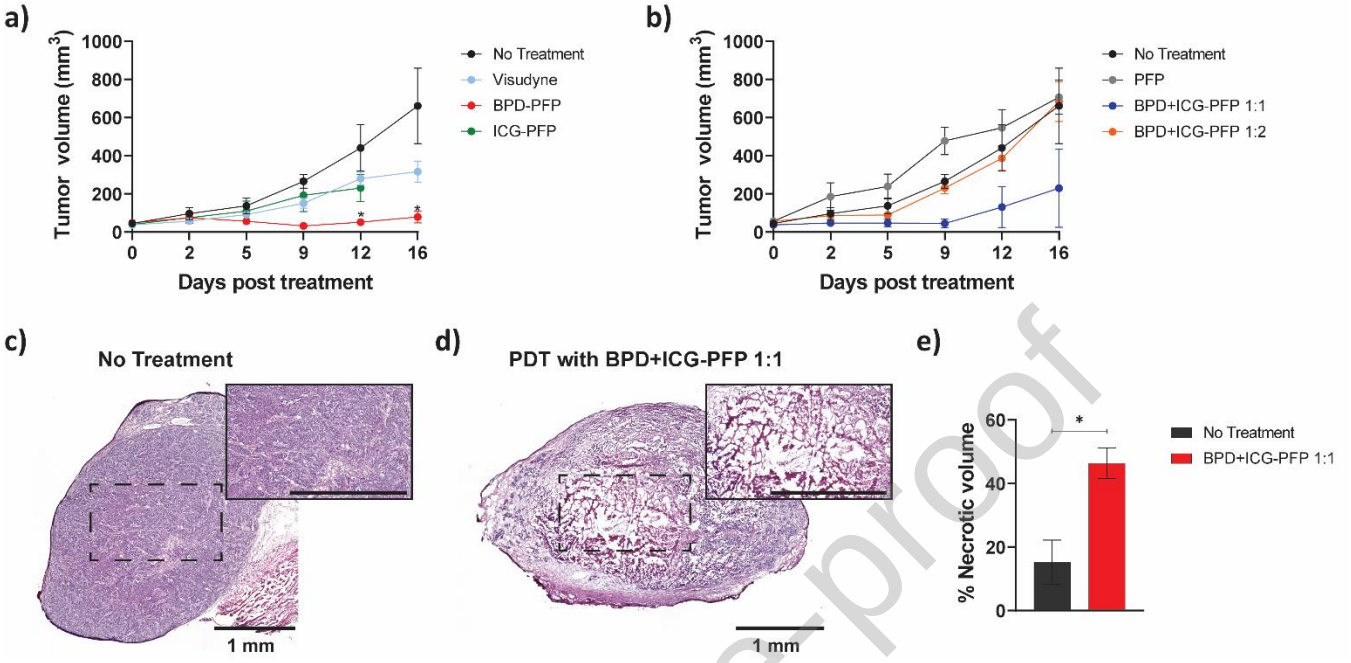

Figure 11: Change in tumor volume in response to PDT treatment with nanodroplet variants. a) Oxygen enhanced BPD-PFP (red line) is significantly efficacious than the clinically used formulation of BPD i.e., Visudyne (cyan line). The tumor volume in the no-treatment group are shown in black line. ICG-PFP nanodroplets had minimal therapeutic effect. b) The tumor volume of the mice in the PFP only group are shown in gray line. The ratio of BPD:ICG ratio within the nanodroplets is critical to achieve effective therapeutic outcome. BPD:ICG 1:1 formulation (blue line) had better efficacy than the BPD:ICG 1:2 formulation (orange line). The H&E image of the tumors in c) non-treated group and d) 24 hours post PDT with BPD+ICG-PFP 1:1 nanodroplets group. The insets show the tumor core at higher magnification. Scale bar in the inset = 1 mm. e) Quantification of necrotic regions in the tumors show higher values in the PDT with BPD+ICG-PFP 1:1 nanodroplets group compared to the control group. The results are expressed as mean ± S.E.M; n = 3-4 mice per group ; Two-way ANOVA with Tukey's multiple comparison test: * = $p < 0.05$.

Graphical abstract

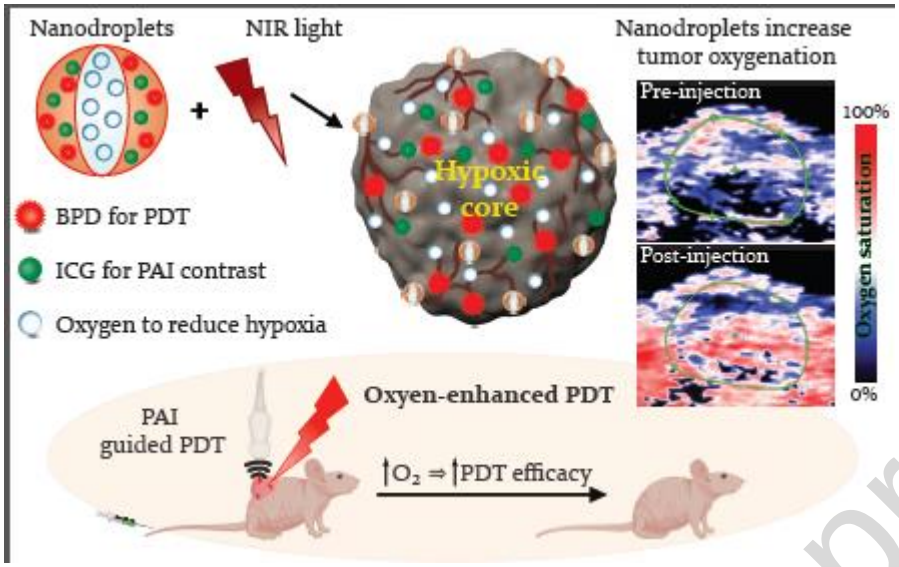

Author Biography will be provided upon acceptance of the manuscript

Declaration of interests

☒ The authors declare that they have no known competing financial interests or personal relationships that could have appeared to influence the work reported in this paper.

☐The authors declare the following financial interests/personal relationships which may be considered as potential competing interests: